Provided for non-commercial research and education use.
Not for reproduction, distribution or commercial use.

This article appeared in a journal published by Elsevier. The attached copy is furnished to the author for internal non-commercial research and education use, including for instruction at the authors institution and sharing with colleagues.

Other uses, including reproduction and distribution, or selling or licensing copies, or posting to personal, institutional or third party websites are prohibited.

In most cases authors are permitted to post their version of the article (e.g. in Word or Tex form) to their personal website or institutional repository. Authors requiring further information regarding Elsevier's archiving and manuscript policies are encouraged to visit:

http://www.elsevier.com/copyright

Author's personal copy

Applied Surface Science 255 (2008) 819–823

Contents lists available at ScienceDirect

Applied Surface Science

journal homepage: www.elsevier.com/locate/apsusc

C_{60} sputtering of organics: A study using TOF-SIMS, XPS and nanoindentation

Gregory L. Fisher [a,*], Michelle Dickinson [b], Scott R. Bryan [a], John Moulder [a]

[a] Physical Electronics, Inc., 18725 Lake Drive East, Chanhassen, MN 55317, United States
[b] Hysitron, Inc., 10025 Valley View Road, Eden Prairie, MN 55344, United States

ARTICLE INFO

Article history:
Available online 15 May 2008

Keywords:
TOF-SIMS
C_{60}
Poly(methyl methacrylate) (PMMA)
Polymer

ABSTRACT

Sputtering of organic materials using a C_{60} primary ion beam has been demonstrated to produce significantly less accumulated damage compared to sputtering with monatomic and atomic-cluster ion beams. However, much about the dynamics of C_{60} sputtering remains to be understood. We introduce data regarding the dynamics of C_{60} sputtering by evaluating TOF-SIMS depth profiles of bulk poly(methyl methacrylate) (PMMA). Bulk PMMA provides an ideal test matrix with which to probe C_{60} sputter dynamics because there is a region of steady-state secondary ion yield followed by irreversible signal degradation. C_{60} sputtering of PMMA is evaluated as a function of incident ion kinetic energy using 10 keV C_{60}^{+}, 20 keV C_{60}^{+} and 40 keV C_{60}^{++} primary ions. Changes in PMMA chemistry, carbon accumulation and graphitization, and topography as a function of total C_{60} ion dose at each accelerating potential is addressed.

© 2008 Elsevier B.V. All rights reserved.

1. Introduction

Pulsed C_{60} ion probes have been applied with increasing frequency in the time-of-flight secondary ion mass spectrometry (TOF-SIMS) analysis of organic and biological materials. The advent of C_{60} sputtering in TOF-SIMS was initially driven by the analytical necessity to affect maximum enhancement in high m/z, molecular, or quasi-molecular ion formation [1,2]. In addition, the sputtering of organic materials using a C_{60} primary ion beam has been demonstrated to produce significantly less accumulated damage compared to sputtering with monatomic and atomic-cluster ion beams. That is to say, in TOF-SIMS analyses utilizing a C_{60} primary ion beam, the fundamental limitation imposed by the static limit may often be disregarded [1–3]. This discovery has enabled molecular depth profiling of organic materials because the structural integrity of the organic analyte(s) remains, in many instances, virtually undisturbed [3,4]. However, while the utilization of C_{60} sputtering has extended the application of TOF-SIMS, much about the dynamics of C_{60} sputtering is not well understood.

In this article, we present data regarding TOF-SIMS depth profiles of C_{60}-sputtered bulk poly(methyl methacrylate) (PMMA), as well as X-ray photoelectron spectroscopy (XPS) and nanoindentation analysis of the C_{60} sputter craters. Bulk PMMA provides an ideal test matrix with which to probe C_{60} sputter dynamics because there is a region of steady-state secondary ion yield followed by irreversible signal degradation. C_{60} sputtering of PMMA is evaluated as a function of incident ion kinetic energy using 10 keV C_{60}^{+}, 20 keV C_{60}^{+} and 40 keV C_{60}^{++} primary ions. By combining the quantitative chemical state information obtained by XPS with the structural information obtained by TOF-SIMS and the mechanical properties afforded by nanoindentation, we gain significant insight to the C_{60} sputtering process. Preliminary observations concerning the correlations between chemical and mechanical properties as a function of sputter ion dose are presented and discussed. We specifically address changes in matrix chemistry, carbon accumulation and graphitization, and topography as a function of total C_{60} ion dose at each accelerating potential. The experimental data presented here provide a glimpse into the mechanism(s) of organic depth profiling with C_{60} primary ions.

2. Experimental

2.1. Samples

Experimental samples of approximately 3/4-in. square were cut from a 1/8-in. thick sheet of commercially available Plexiglass. The protective film was peeled from the experimental samples to expose the bulk PMMA material for analysis. TOF-SIMS analyses revealed a surface layer of silicone residue. The silicone residue may be nominally removed using a lint-free cloth, or wiper, and isopropanol. Nitrile gloves and isopropanol-cleaned tools were used for all sample handling.

* Corresponding author.
E-mail address: gfisher@phi.com (G.L. Fisher).

0169-4332/$ – see front matter © 2008 Elsevier B.V. All rights reserved.
doi:10.1016/j.apsusc.2008.05.182

Author's personal copy

2.2. TOF-SIMS analysis

TOF-SIMS depth profiles and analysis were performed using a TRIFT V nanoTOF (Physical Electronics, Chanhassen, MN) instrument equipped with a 20 kV C_{60} primary ion gun. The C_{60} ion optics column is oriented 48° from surface normal. The instrument is equipped with a turbomolecular-pumped fast sample entry chamber and a turbomolecular-pumped analysis chamber having a base pressure of $\sim 5 \times 10^{-10}$ Torr. The fast sample entry was pumped down to $< 5 \times 10^{-6}$ Torr before the samples were transferred to the analytical chamber.

The C_{60} primary ion gun and associated electronics are configured such that C_{60} ions may be used for both the sputtering and the analysis phases of the depth profile. The dc current of C_{60} primary ions delivered to the sample was 1 nA; this dc current is relatively consistent at the three accelerating potentials of 10 keV C_{60}^{+}, 20 keV C_{60}^{+} and 40 keV C_{60}^{++}. Raster sizes of 300 μm × 300 μm and 20 μm × 20 μm were used for sputtering and analysis, respectively. Each sputter cycle was 60 s in duration delivering a dose of 4.2×10^{14} C_{60}/cm^2 to the sample. Each analytical cycle was 30 s in duration delivering a dose of 1.2×10^{12} C_{60}/cm^2 to the sample. Mass spectra were collected in the mass-to-charge (m/z) range of 0–1850 m/z, in the negative polarity only, during the depth profile experiments. Charge compensation was accomplished during spectrum acquisition using 10 eV electrons; no charge compensation was used while sputtering. The sputter depth profiles were carried out at each accelerating potential to a nominal order-of-magnitude drop in secondary ion signal of the 85 m/z ($C_4H_5O_2^-$) and 185 m/z ($C_9H_{13}O_4^-$) fragments of PMMA.

2.3. Nanoindentation

Nanoindentation was performed approximately 8 weeks following the TOF-SIMS depth profile analysis using a TriboIndenter (Hysitron, Inc., Eden Prairie, MN) consisting of a nanoindentation transducer with a Berkovich (three-sided pyramid) diamond indenter tip and a scanning probe microscope. The nanoindenter was equipped with a dynamic testing module (nanoDMA II; Hysitron, Inc.) to superimpose a small sinusoidal load on the quasistatic load during nanoindentation testing. Before testing, the shape of the indenter tip was characterized using the method of Oliver and Pharr [5]. Load-controlled indentations were made along the sample surface in regions identified with the attached optical microscope. The indentation modulus, E_i, and the hardness, H, were calculated from the unloading portion of the load displacement data.

Dynamic indentation tests were performed on each sample. The dynamic testing scheme differed from the quasistatic testing by a small, sinusoidally varying load superposed at 100 Hz on the constant load of 1000 μN. During the mapping process, the dynamic test is performed by oscillating the indenter tip with small forces while monitoring the resultant displacement and phase lag due to the material response. Simultaneously, scanning probe microscopy (SPM) imaging allows the indenter tip to scan across the material surface. The system continuously monitors the stiffness of the sample and provides a plot of the stiffness as a function of the position on the sample. The stiffness is given at each pixel of the image, and the modulus can be calculated if the geometry of the probe tip is known. The complex modulus information obtained by this modulus mapping technique includes the real and imaginary parts, $E = E' + iE''$, and provides the storage and loss characteristics of the material. The results of the modulus mapping are equivalent to a dynamic indentation test performed at each pixel in a 256 × 256 image.

2.4. XPS analysis

XPS analysis of the PMMA samples occurred following analysis by nanoindentation. XPS spectra were obtained using a Quantera scanning XPS microprobe (Physical Electronics, Chanhassen, MN). The C_{60} sputter craters were pre-located optically using the Quantera's Sample Positioning Station. Location of the sputter craters was verified inside the instrument using X-ray beam-induced secondary electron images. The X-ray beam used for these measurements was a 15 keV, 12 W, monochromatic Al Kα X-ray beam that was 50 μm in diameter. Survey spectra were obtained operating the energy analyzer at a 280 eV pass energy and high energy resolution C 1s spectra were obtained using a 13 eV pass energy. Charge neutralization was performed using a combination of 1 eV electrons and 6 eV Ar^{+} ions.

3. Results and discussion

At each C_{60} accelerating potential, i.e. 10 keV C_{60}^{+}, 20 keV C_{60}^{+} and 40 keV C_{60}^{++}, TOF-SIMS depth profiles were carried out to approximately one order-of-magnitude loss of signal at 85 and 185 m/z. The results of the TOF-SIMS depth profiles are rendered in Fig. 1. The normalized data at 85 m/z (Fig. 1A) and at 185 m/z (Fig. 1B) are plotted against the sputter depth for each C_{60} accelerating potential. The average crater depths were determined by profilometry to be 0.6, 1.3 and 2.8 μm at 10 keV C_{60}^{+}, 20 keV C_{60}^{+} and 40 keV C_{60}^{++}, respectively. The sputter depth in this initial experiment was not well controlled; nevertheless, a plot of crater depth versus beam energy indicates an approximately linear relationship. These results are sufficient to demonstrate significant

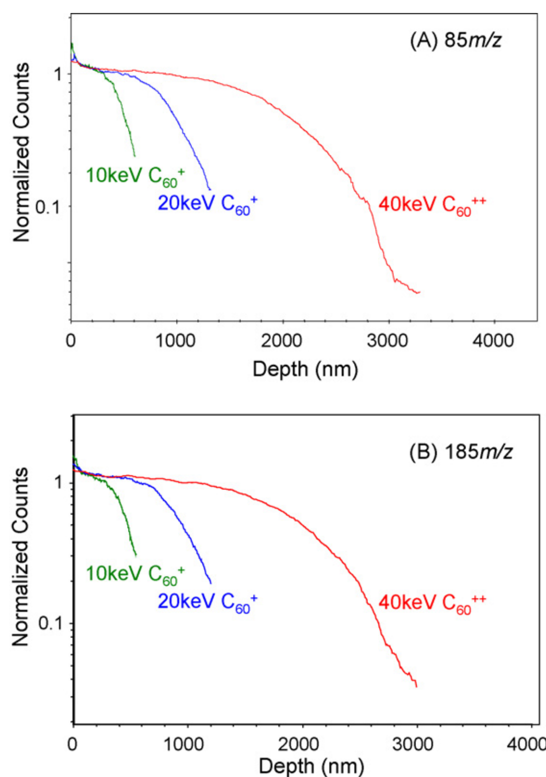

Fig. 1. Negative TOF-SIMS depth profiles of bulk PMMA generated using 10 keV C_{60}^{+} (green), 20 keV C_{60}^{+} (blue) and 40 keV C_{60}^{++} (red) primary ions for both sputtering and acquisition. (A) Normalized counts at 85 m/z plotted against sputter depth. (B) Normalized counts at 185 m/z plotted against sputter depth. (For interpretation of the references to color in this figure legend, the reader is referred to the web version of the article.)

Author's personal copy

Table 1
Contact depth (1000 μN maximum load), elastic modulus and hardness (100 nm sampling depth) acquired within each C_{60} sputter crater and from an unsputtered reference area

Sample	Contact depth (nm)	Modulus (GPa)	Hardness (GPa)
Reference	341.05 ± 1.70	5.18 ± 0.0241	0.3188 ± 0.0030
10 keV C_{60}^{+}	349.12 ± 12.46	5.25 ± 0.1978	0.3059 ± 0.0208
20 keV C_{60}^{+}	393.64 ± 36.21	5.36 ± 0.7781	0.2477 ± 0.0444
40 keV C_{60}^{++}	740.98 ± 75.13	3.34 ± 0.2512	0.0738 ± 0.0160

differences in the properties of the sputtered material at each kinetic energy.

Variation in the mechanical properties of C_{60}-sputtered PMMA was probed by nanoindentation. The mean values and standard deviations for contact depth, elastic modulus and hardness, at each C_{60} accelerating potential, are displayed in Table 1. Reference values for each parameter were acquired at an unsputtered portion of the same sample. The contact depth was measured to a maximum load of 1000 μN; the top-most 100 nm of material at the crater base was sampled to determine the elastic modulus and hardness. These data indicate that the mechanical properties of C_{60}-sputtered PMMA remain relatively unchanged with respect to the unsputtered PMMA, within the measurement error, at the 10 keV C_{60}^{+} and 20 keV C_{60}^{+} accelerating potentials. A significant change is observed within the PMMA matrix that was sputtered with 40 keV C_{60}^{++}. It is noteworthy to mention that the contact depth of the 40 keV C_{60}^{++} sputter crater is more than twice that of the reference area. Moreover, the hardness is reduced by more than three times with respect to the reference area. These data indicate that the 40 keV C_{60}^{++}-sputtered polymer matrix has been disrupted; that is to say, the average molecular weight is reduced [6].

Topography and complex modulus images were also acquired by nanoindentation and are given in Figs. 2 and 3, respectively. Within each C_{60} sputter crater, and at an unsputtered area of the surface, the topography and the complex modulus were imaged simultaneously within a 10 μm × 10 μm area. During these measurements, only 1 nm of surface material is sampled. These images reveal a peak-to-peak roughness of ~6 nm and an average complex modulus of ~20 GPa for the unsputtered PMMA. Within the 10 keV C_{60}^{+} sputter crater, the peak-to-peak roughness increases to ~57 nm and the average complex modulus decreases slightly to ~18 GPa. At the 20 keV C_{60}^{+} accelerating potential, the peak-to-peak roughness increases again to ~183 nm while the average complex modulus decreases to ~16 GPa. Finally, at the 40 keV C_{60}^{++} accelerating potential, the peak-to-peak roughness increases to ~309 nm and the average complex modulus decreases significantly to ~10 GPa.

The increasing roughness at the crater base as a function of C_{60} kinetic energy is particularly noteworthy. It has been shown that, during steady-state sputtering with C_{60}, a uniform crater base is formed [2,3]. It may then follow that, for material systems where steady-state sputtering during TOF-SIMS analysis is followed by secondary ion signal degradation, that the crater base would have a roughness that is independent of accelerating potential. That is to say, following steady-state sputtering at different C_{60} kinetic energies, if sputtering is continued to a uniform loss of secondary ion signal, that the crater bases might be expected to have similar

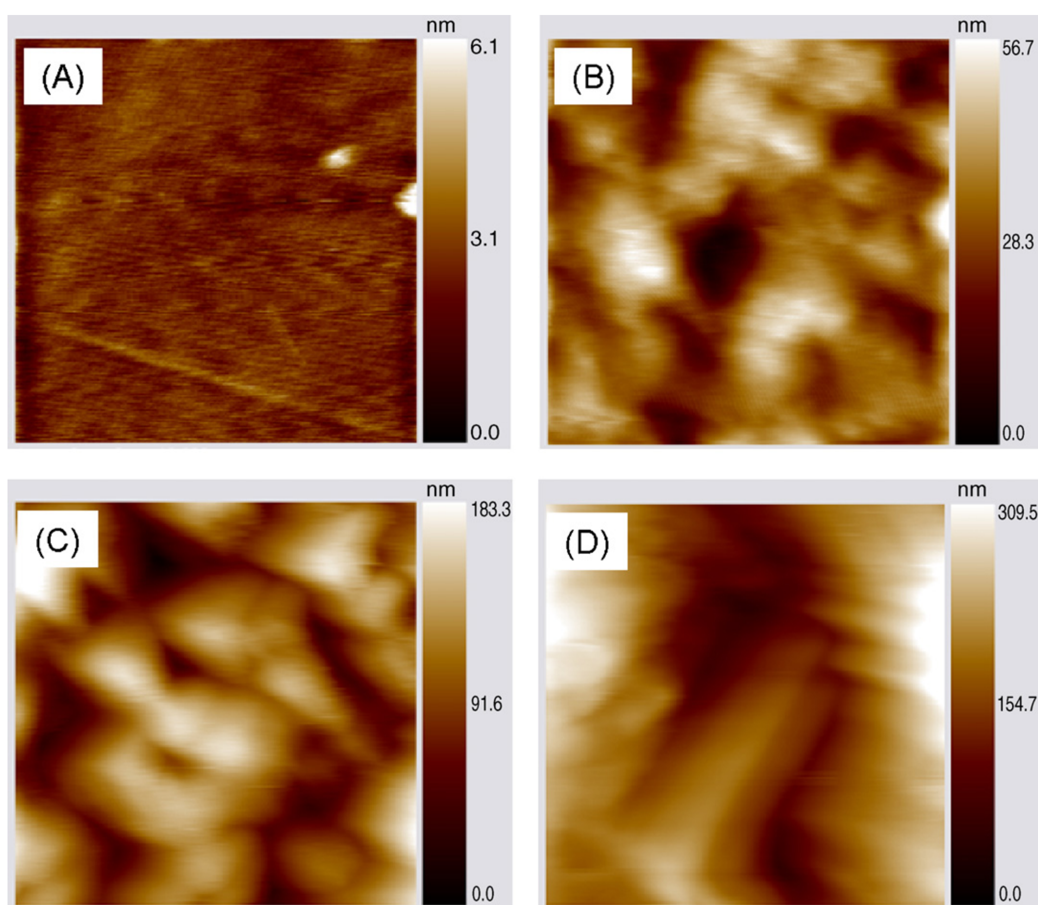

Fig. 2. Topographical images acquired by nanoindentation. Each plot shows a 10 μm × 10 μm area. (A) Reference area. (B) 10 keV C_{60}^{+} sputter crater. (C) 20 keV C_{60}^{+} sputter crater. (D) 40 keV C_{60}^{++} sputter crater.

Author's personal copy

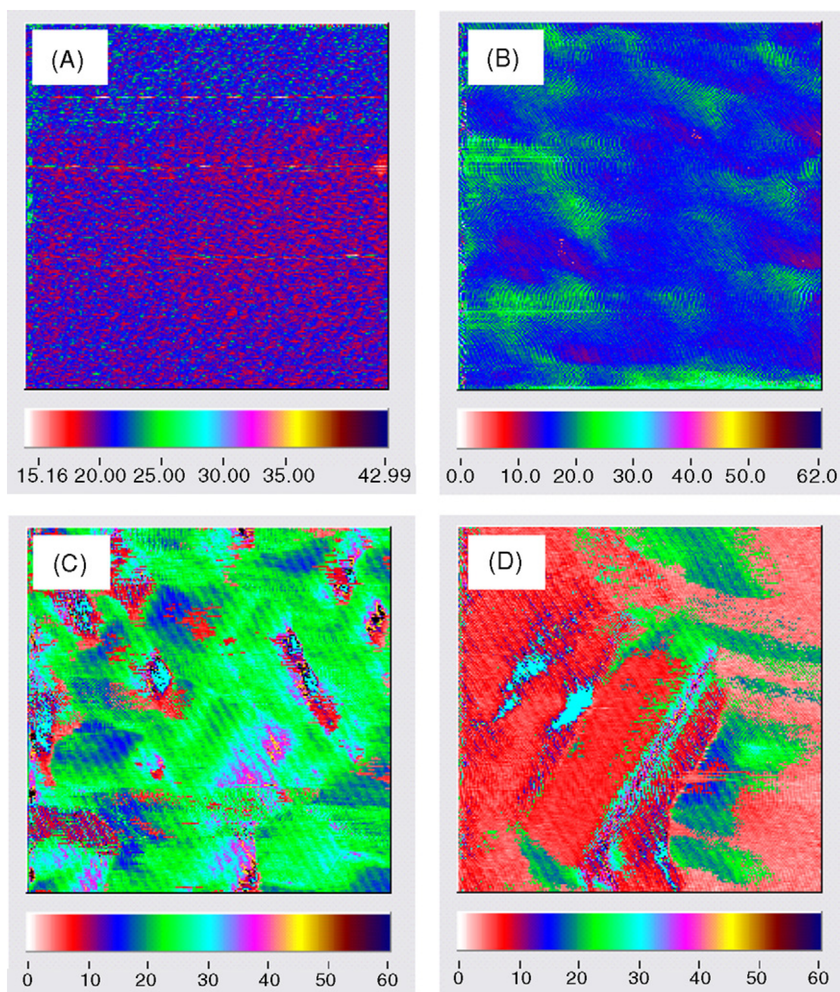

Fig. 3. Complex modulus maps acquired by nanoindentation. Each plot shows a 10 μm × 10 μm area. (A) Reference area. (B) 10 keV C_{60}^{+} sputter crater. (C) 20 keV C_{60}^{+} sputter crater. (D) 40 keV C_{60}^{++} sputter crater.

roughnesses. Indeed, we have some data, not reported here due to the incomplete nature of the investigation, that suggests this to be the case [7]. Therefore, we posit that intrinsic defects and microcrystalline domains within the bulk PMMA used for this study may be the primary source of the increasing roughness as a function of sputtered depth. To be succinct, inclusions and defects within the bulk of the polymer initiate preferential sputtering that is exacerbated as the sputter depth increases. This subject is still under investigation and will be fully discussed in a future article.

High resolution XPS spectra were collected from a 50 μm spot within each C_{60}-generated sputter crater and at an unsputtered portion of the sample. The C 1s spectra at each sample location are given in Fig. 4. These data reveal two important features concerning the C_{60}-sputtered craters as a function of kinetic energy. First, the PMMA chemistry is increasingly disrupted with increasing sputter depth. The disruption of the PMMA functional groups is noted by decreasing O–*C*═O and O–*C*H$_3$ C 1s signals as a function of crater depth, or C_{60} kinetic energy. It is difficult at this point to determine whether this observation is the result of C_{60} accelerating potential, sputtered depth (i.e. total ion dose), or both. Again, this subject is currently under examination by sputtering to the same nominal depth, or nominal primary ion dose, with the different C_{60} kinetic energies. Sputtering to the same nominal depth requires a greater primary ion dose at low kinetic energy than at high kinetic energy.

The second important observation derived from the XPS data is that there is no significant accumulation of carbon, graphitic or otherwise, within the C_{60} sputter craters. Graphitic carbon would be manifest by a C 1s shift to lower binding energy. No such shift is

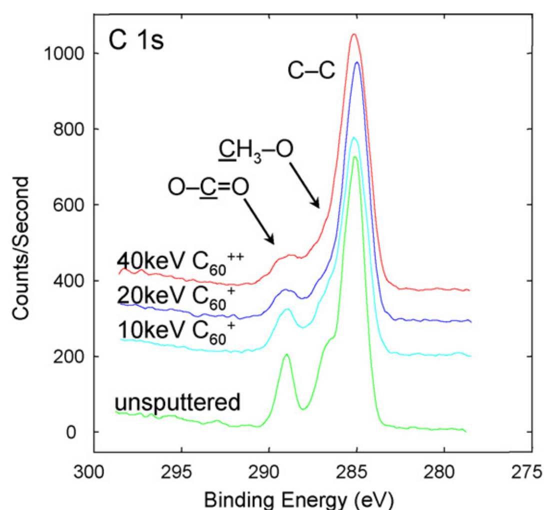

Fig. 4. Overlayed plots of high resolution XPS spectra showing the C 1s region.

Author's personal copy

Table 2
Integrated areas of the C 1s and O 1s regions of the high resolution XPS spectra acquired within each C_{60} sputter crater and from an unsputtered reference area

	Ref. area (%)	10 keVC_{60}^{+} (%)	20 keV C_{60}^{+} (%)	40 keV C_{60}^{++} (%)
Carbon	73.5	77.3	83.0	81.7
Oxygen	25.0	20.6	16.2	17.4
Other	1.6	2.1	0.8	0.8

evident. Furthermore, the total carbon, determined as area under the C 1s peak, remains relatively consistent for the C_{60} kinetic energies that were evaluated. The carbon and oxygen content of sputter craters at each C_{60} kinetic energy are summarized in Table 2. The corresponding values from an unsputtered reference area are also given. It was expected that carbon accumulation would be observed within each C_{60} sputter crater. It has been reported that carbon accumulation is an outcome of C_{60} sputtering that results in decreased sputter yield, decreased secondary ion yield and increased topography [8]. Moreover, the sputter craters of our samples appeared optically dark indicating the possibility of carbon accumulation. However, in light of the data reported here and more recent experimental results, the dark appearance of the PMMA sputter craters may be attributed to topographical roughness which, in turn, may be the result of defects inherent in the experimental samples.

Together, these data shed some light on the C_{60} sputtering dynamics of organic solids. Since little or no carbon accumulation is evident, the falloff in TOF-SIMS secondary ion signal must be the result of topographically induced sputter yield degradation. The topography ostensibly originates at intrinsic defects and microcrystalline domains within the experimental PMMA samples which induce and accelerate preferential sputtering.

Chemical degradation is made evident by both XPS and nanoindentation. Namely, the carbonyl and ether linkages are deteriorated and the average molecular weight is decreased as a function of crater depth. We surmise that this accumulation of sputter-induced damage is also related to topography and is not an attribute of sputtering at higher C_{60} kinetic energies. The effectiveness of C_{60} sputtering, specifically as it relates to molecular depth profiling, lies in the ability of an incident C_{60} ion to remove sputter-induced damage created by the preceding C_{60} ion [2,3,9,10]. The figure of merit for steady-state molecular depth profiling requires that the sputter depth over the range is greater than one [2–4,9–11]. Indeed, it may be argued using the data presented in this article that the higher energy C_{60} primary ions more efficiently remove sputter-induced damage. This statement is supported by the fact that each successive increase in C_{60} kinetic energy results in a crater depth more than twice that of the lower energy, in spite of the increased topography.

Experiments are currently underway to disentangle the effects of C_{60} kinetic energy from ion dose and materials-related artifacts. Artifacts arising from experimental specimens will be minimized by using CQ-grade PMMA. Chemical and mechanical properties will be probed while controlling the experiments, in turn, for total ion dose or crater depth at each discrete C_{60} accelerating potential (i.e. 10, 20 and 40 keV). In addition, this methodology should allow any significant variation in sputter rate, or yield, as a function of total ion dose to be observed.

4. Conclusions

We have embarked on an experimental path to unravel the dynamics of C_{60} sputtering with respect to C_{60} accelerating potential. The experimental data show both subtle and gross changes in the chemical and the mechanical properties of C_{60}-sputtered bulk PMMA, about which the significance is blurred by topographical features. However, two assertions are made in light of this and previous work. First, neither carbon accumulation within the C_{60} sputter crater nor graphitization of the polymer matrix was observed and, therefore, cannot be the cause of declining TOF-SIMS secondary ion signal. Second, sputtering with C_{60} at higher accelerating potentials more effectively removes sputter-induced damage and prolongs steady-state molecular depth profiling. Investigations are continuing, as briefly described above, in an effort to fully disentangle the dynamics of C_{60} sputtering.

References

[1] N. Winograd, Anal. Chem. 77 (2005) 143A.
[2] N. Winograd, Z. Postawa, J. Cheng, C. Szakal, J. Kozole, B. Garrison, Appl. Surf. Sci. 252 (2006) 6836.
[3] J. Cheng, A. Wucher, N. Winograd, J. Phys. Chem. B110 (2006) 8329.
[4] J.S. Fletcher, X.A. Conlan, E.A. Jones, G. Biddulph, N.P. Lockyer, J.C. Vickerman, Anal. Chem. 78 (2006) 1827.
[5] W.C. Oliver, G.M. Pharr, J. Mater. Res. 7 (1992) 1564.
[6] E.H. Lee, G.R. Rao, L.K. Mansur, Trends Polym. Sci. 4 (1996) 229.
[7] We have just recently probed a partial set of experimental samples, the results of which indicate that sputter crater roughness is independent of kinetic energy. Also, see citations [3] and [9–11].
[8] G. Gillen, J. Battaes, C.A. Michaels, P. Chi, J. Small, E. Windsor, A. Fahey, J. Verkouteren, K.J. Kim, Appl. Surf. Sci. 252 (2006) 6521.
[9] Z. Postawa, B. Czerwinski, M. Szewczyk, E.J. Smiley, N. Winograd, B.J. Garrison, J. Phys. Chem. B108 (2004) 7831.
[10] A. Delcorte, Phys. Chem. Chem. Phys. 7 (2005) 3395.
[11] A. Delcorte, B.J. Garrison, Nucl. Instr. Meth. Phys. Res. B225 (2007) 223.